A&A 505, 45–53 (2009)
DOI: 10.1051/0004-6361/200912301

Astronomy & Astrophysics

Testing the radio halo-cluster merger scenario

The case of RXC J2003.5–2323

S. Giacintucci[1,2], T. Venturi[2], G. Brunetti[2], D. Dallacasa[3,2], P. Mazzotta[4,1], R. Cassano[2], S. Bardelli[5], and E. Zucca[5]

[1] Harvard-Smithsonian Centre for Astrophysics, 60 Garden Street, Cambridge, MA 02138, USA
[2] INAF - Istituto di Radioastronomia, via Gobetti 101, 40129, Bologna, Italy
e-mail: tventuri@ira.inaf.it
[3] Dipartimento di Fisica, Università di Roma Tor Vergata, via della Ricerca Scientifica 1, 00133, Roma, Italy
[4] Dipartimento di Astronomia, Universitá di Bologna, via Ranzani 1, 40127, Bologna, Italy
[5] INAF - Osservatorio Astronomico di Bologna, via Ranzani 1, 40127, Bologna, Italy

Received 8 April 2009 / Accepted 15 May 2009

ABSTRACT

Aims. We present a combined radio, X-ray, and optical study of the galaxy cluster RXC J2003.5–2323. The cluster hosts one of the largest, most powerful, and distant giant radio halos known to date, suggesting that it may be undergoing a strong merger. The aim of our multiwavelength study is to investigate the radio-halo cluster merger scenario.
Methods. We studied the radio properties of the giant radio halo in RXC J2003.5–2323 by means of new radio data obtained at 1.4 GHz with the Very Large Array, and at 240 MHz with the Giant Metrewave Radio Telescope, in combination with previously published GMRT data at 610 MHz. The dynamical state of the cluster was investigated by means of X-ray *Chandra* observations and optical ESO-NTT observations.
Results. Our study confirms that RXC J2003.5–2323 is an unrelaxed cluster. The unusual filamentary and clumpy morphology of the radio halo could be due to a combination of the filamentary structure of the magnetic field and turbulence in the inital stage of a cluster merger.

Key words. radiation mechanisms: non-thermal – galaxies: clusters: general – galaxies: clusters: individual: RXC J2003.5–2323

1. Introduction

RXC J2003.5–2323 is an X-ray luminous and massive galaxy cluster at redshift $z = 0.317$, belonging to the ROSAT-ESO Flux Limited X-ray cluster catalogue (REFLEX; Böhringer et al. 2004). Its main properties are summarized in Table 1. RXC J2003.5–2323 hosts a cluster scale radio source classified as a giant radio halo (Venturi et al. 2007, hereinafter VGB07).

Radio halos are diffuse, cluster-scale low surface brightness radio sources of synchrotron origin found in a fraction of X-ray luminous (i.e. massive) clusters. They are not associated with individual galaxies but rather with the intracluster medium itself, and provide direct evidence of relativistic particles and μG magnetic fields in galaxy clusters (see Ferrari et al. 2008, for a recent review).

The giant radio halo in RXC J2003.5–2323 was discovered by observations carried out at 610 MHz with the Giant Metrewave Radio Telescope (GMRT) as part of the GMRT Radio Halo Survey (VGB07 and Venturi et al. 2008, hereinafter VGD08), devoted to a statistical study of diffuse radio emission in a complete sample of galaxy clusters in the redshift range $z = 0.2$–0.4. With a largest linear size of ∼1.4 Mpc and a total radio power of $\log P_{610\ \mathrm{MHz}}$ (W Hz^{-1}) = 25.53, this source is among the largest, most powerful, and most distant halos known to date. The radio halo in RXC J2003.5–2323 has a complex morphology, with clumps and filaments extending over hundreds of kpc, an uncommon feature of radio halos, which generally show a fairly regular and homogeneous radio brightness distribution (VGB07). Its peculiar radio emission is reminiscent of the giant radio halo in A 2255 ($z = 0.08$), whose emission has a filamentary structure, lengthscale of ∼550 kpc and fractional polarization at levels of ∼20–40% (Govoni et al. 2005). To date, A 2255 is the only known radio halo with polarized emission.

The origin of giant radio halos in clusters has long been debated, since the lifetime of the relativistic electrons responsible for the synchrotron radio emission is much shorter than the diffusion time necessary to cover their Mpc extent, therefore some form of re-acceleration is required. Among the possible models proposed, the re-acceleration scenario (Brunetti et al. 2001; Petrosian 2001), which requires that electrons are in situ re-accelerated by turbulence injected in the intracluster medium (ICM) by a recent or ongoing cluster major merger event, has received wide support (Feretti 2003; and Brunetti 2008; and Cassano 2009, for reviews).

Table 1. General properties of RXC J2003.5–2323.

RA_{J2000}	20h03m30.4s
Dec_{J2000}	−23°23′05″
z	0.317
$L_{\mathrm{X}\,[0.1-2.4\ \mathrm{keV}]}$	9.25×10^{44} erg s^{-1} (a)
M_{V}	$2.05 \times 10^{15}\ M_{\odot}$ (b)
R_{V}	2.75 Mpc (b)

Notes to Table 1: (a) Böhringer et al. (2004); (b) virial Mass M_{V} and virial radius R_{V} from the $L_{\mathrm{X}\,[0.1-2.4\ \mathrm{keV}]} - M_{\mathrm{V}}$ relation in Cassano et al. (2006).

Table 2. Summary of the radio observations.

Telescope	Observation date	ν (MHz)	$\Delta\nu$ (MHz)	t (min)	*HPBW*, PA (full array, $''\times''$, $^\circ$)	rms (μJy b^{-1})	u–v range ($k\lambda$)	LDS ($'$)
VLA–CnB	9, 30 Oct. 2006	1400	25	540	12.6×9.2, 85	20	~0.27–26.5	7
GMRT	3 Jun. 2007	240	8	240	31.6×10.8, 52	290	~0.04–20.5	44

A connection between radio halos and mergers is suggested by radio observations. An analysis of the clusters with sensitive radio and X-ray imaging shows that all clusters hosting a radio halo show signs of ongoing mergers, while those without a halo may be either perturbed or relaxed (Buote 2001; Govoni et al. 2004; VGD08 and references therein). In the case of RXC J2003.5–2323, the sparse information available in the literature and public archives, both in the X-ray and optical bands, was insufficient to derive its dynamical properties (VGB07).

To test the merger-halo connection, we carried out *Chandra* X-ray and ESO New Technology Telescope (NTT) optical observations, to study the dynamics of the ICM (which represents the collisional part) and of the cluster galaxy population (essentially collisionless). Moreover, we observed the cluster with the GMRT at 240 MHz and with the Very Large Array (VLA) at 1.4 GHz, to derive the radio spectral properties of the halo.

In this paper, we report on the new multi-band observations. The radio observations and data reduction are described in Sect. 2, and their results and analysis are reported in Sect. 3; the *Chandra* observations and analysis are described in Sect. 4; the ESO-NTT optical observations are presented in Sect. 5; results are presented and discussed in Sect. 6; summary and conclusions are given in Sect. 7.

We adopt the ΛCDM cosmology with $H_0 = 70$ km s^{-1} Mpc^{-1}, $\Omega_m = 0.3$ and $\Omega_\Lambda = 0.7$. At the redshift of RXC J2003.5–2323 ($z = 0.317$), this cosmology corresponds to a linear scale of $1'' = 4.62$ kpc. The spectral index α is defined according to $S \propto \nu^{-\alpha}$. All the error ranges are 90% confidence intervals, unless stated otherwise.

2. Radio observations and data reduction

To derive the spectrum of the giant radio halo in RXC J2003.5–2323 with at least three data points and investigate its polarization properties, we observed the cluster at 1.4 GHz with the VLA and at 240 MHz with the GMRT. The details of all the observations are summarized in Table 2, where we provide the observing date, frequency, total bandwidth, total time on source, half power bandwidth (*HPBW*) and rms level (1σ) in the full resolution images, u–v range, and largest detectable structure (LDS).

2.1. VLA 1.4 GHz observations

The 1.4 GHz observations were carried out in October 2006 with the VLA in the hybrid CnB configuration to optimize the u–v coverage at the low declination of the source. We observed the halo in two different runs, for a total integration time of ~9 h on source (Table 2). The standard polarization mode at 1.4 GHz was used during the observations. The data were collected in spectral-line mode to filter out the radio frequency interference in the observing band more effectively, and properly image the entire cluster field with wide-field imaging. We used 8 channels for each of the two IFs, centered on 1385 MHz and 1465 MHz, with a total bandwidth of 25 MHz/IF. Both 3C 286 and 3C 343 were observed for the bandpass and primary flux density calibration, and for the calibration of the polarization electric vector. The phase calibration was obtained from the nearby calibrator 1923–210, while multiple observations of 1949–199 over a large range of parallactic angles were used to calibrate the instrumental polarization. Calibration and imaging were performed using the National Radio Astronomy Observatory (NRAO) Astronomical Image Processing System (AIPS) package.

The datasets from the two different days were calibrated separately. After bandpass calibration, the 8 channels/IF of each dataset were averaged to 1 single channel of ~22 MHz. Each dataset was self-calibrated in phase only, implementing the wide-field imaging faceting technique to compensate for non-coplanarity. We used a total of 18 facets to cover the primary beam area and bright outlying sources. The final self-calibrated datasets were then combined together to produce the final images.

Both uniform and natural weighting were used for the total intensity image I, and for the images in the Stokes parameters Q and U. The polarized intensity images were derived from the Q and U images. A high sensitivity ($1\sigma = 20$ μJy b^{-1}) was achieved in our final full resolution I image (Table 2). The sensitivity of the U and Q images is $1\sigma = 11$ μJy b^{-1}. The residual amplitude errors are $\lesssim$5%.

2.2. GMRT observations at 240 MHz

RXC J2003.5–2323 was observed using the GMRT at 240 MHz in June 2007 for a total integration time of ~4 h (Table 2). The observations were performed in spectral-line mode using the upper side band (USB) with 128 channels, with a spectral resolution of 62.5 kHz/channel. The total observing band was 8 MHz. During the observations, a number of antennas in the East arm were not available due to a power outage. This led to a very asymmetric beam in the final images produced using the full array (Table 2).

The data calibration and reduction was carried out using AIPS. The bandpass calibration was performed using the primary calibrator. Removal of radio frequency interference (RFI) was carried out using the task FLGIT in AIPS, and by a subsequent careful editing of residual RFI (see Giacintucci et al. 2008, for details). After bandpass calibration, the central 84 channels were averaged to 6 channels of ~0.9 MHz each to reduce the size of the dataset, and at the same time minimize the bandwidth smearing effects within the primary beam. Given the large field of view of the GMRT, 25 facets covering a ~2° × 2° field were used during the imaging in the self-calibration process. After a number of phase self-calibration cycles, the final dataset was averaged from 6 channels to 1 single channel[1]. Despite the limited number of available antennas, we achieved a sensitivity level of

[1] Bandwidth smearing is relevant only at the outskirts of the wide field, and does not significantly affect the region presented and analysed here.

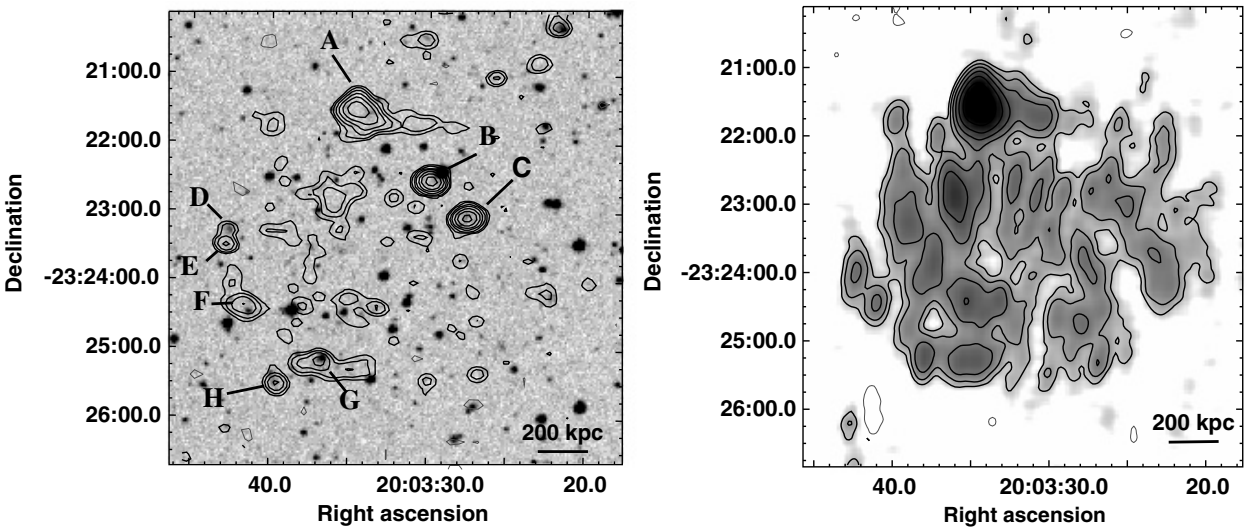

Fig. 1. *Left panel* – full resolution VLA 1.4 GHz contours of the central region of RXC J2003.5–2323, superimposed on the POSS-2 red optical image. The resolution of the radio image is 12.6″ × 9.2″, PA 85°. The 1σ level is 20 μJy/b. Contours are spaced by a factor 2, starting from ±0.06 mJy b^{-1}. Individual sources are labelled from A to H. *Right panel* – VLA 1.4 GHz gray scale and radio contours of the giant radio halo after subtraction of the individual radio galaxies (from B to H in *the left panel*). The resolution is 25.8″ × 13.7″, PA −8°. The 1σ level in the image is 20 μJy b^{-1}. Contours are spaced by a factor 2, starting from ±0.06 mJy b^{-1}.

1σ = 290 μJy b^{-1} in the full resolution image (Table 2). The residual amplitude errors are of the order of $\lesssim$5%.

3. The giant radio halo

3.1. Morphology at 1.4 GHz

The VLA full resolution image at 1.4 GHz of the central region of RXC J2003.5–2323 is presented in the left panel of Fig. 1. The radio contours are overlaid on the POSS-2 red optical image to highlight the discrete radio sources in the cluster region (labelled from A to H), which were also detected in the ∼7″ resolution image at 610 MHz (see Fig. 6 in VGB07). All sources have an optical association except source A, which has no clear counterpart on the POSS-2 image. The nature of A is unclear, as we will be briefly discuss in Sect. 3.4.

Given the high sensitivity of the image, the brightest regions of the diffuse emission from the central part of the radio halo are already clearly visible, despite the inadequate angular resolution. An image of the halo tapered to a resolution of 26″ × 14″ is given in the right panel of Fig. 1. The image was obtained after subtraction of the optically identified radio sources (i.e. B to H).

The halo extends to a total scale of ∼5′, corresponding to a liner size of ∼1.4 Mpc, in very good agreement with the source size at 610 MHz. As observed with the GMRT at 610 MHz (VGB07), the source exhibits a complex and inhomogeneous structure, characterized by bright clumps and filaments of emission (significant at the level of 12σ). In Fig. 2, we compare the halo at 610 MHz (grey scale) and at 1.4 GHz (red contours). The images were produced using the same u–v range (0.2−10 $k\lambda$), and restored with the same beam of 35″ × 35″. The overall size and shape of the source at these two frequencies are in general agreement, although the details of the halo surface brightness distribution, i.e. position of peaks and clumps, differ in the two images. This discrepancy is most likely both observational and intrinsic, i.e. partly due to the different sensitivity and u–v coverage of the two observations, and partly due to a patchy distribution of the spectral index.

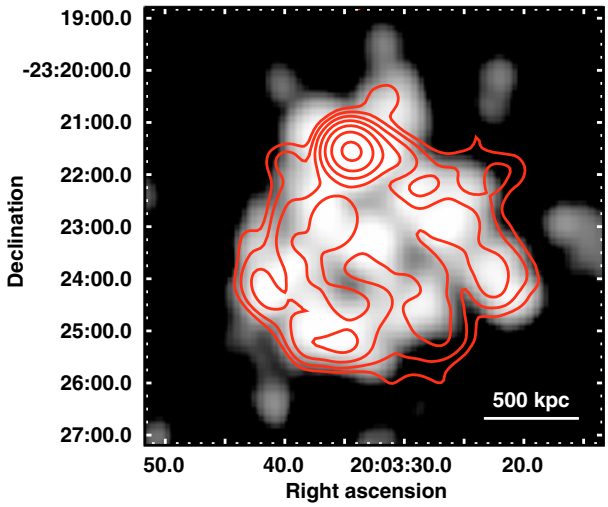

Fig. 2. VLA 1.4 GHz contours (red) of the giant radio halo in RXC J2003.5–2323, superimposed on GMRT 610 MHz image (grey scale). Discrete radio galaxies have been subtracted in both images. The resolution is 35.0″ × 35.0″, PA 0°. The 1σ level is 30 μJy b^{-1} at 1.4 GHz and 100 μJy b^{-1} at 610 MHz. Contours are spaced by a factor 2, starting from ±0.09 mJy b^{-1}.

3.2. The radio halo polarization at 1.4 GHz

The inhomogenous surface brightness distribution of the giant radio halo in RXC J2003.5–2323 is reminiscent of the morphology of the halo in A 2255, where polarized filaments of emission were detected by Govoni et al. (2005) with the VLA at 1.4 GHz, of fractional polarization of the order of ∼20–40%. The upper limit to the polarized emission in the faintest regions of the halo is of the order of $\lesssim$15%.

We used our VLA 1.4 GHz polarimetric observations (Table 2) to search for possible polarized emission associated with the substructures in the surface brightness distribution of the radio halo in RXC J2003.5–2323. We obtained images of the linear polarized intensity from the full resolution Q and

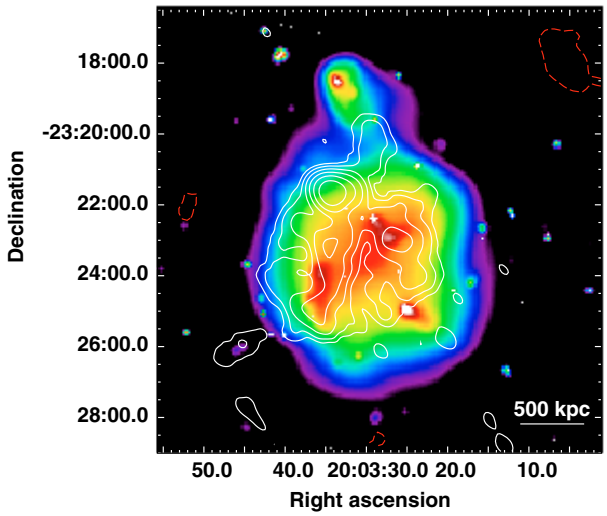

Fig. 3. *Chandra*-GMRT overlay. The X-ray Chandra photon image is background-subtracted, exposure corrected, and binned to 4″ pixels (see Sect. 4), and includes point sources. The GMRT 235 MHz image (contours) of the giant radio halo in RXC J2003.5–2323 was obtained after subtraction of the individual radio galaxies. The resolution is 35.0″ × 35.0″, PA 0°. The 1σ level is 0.4 mJy b^{-1}. Contours are spaced by a factor 2, starting from ±1.2 mJy b^{-1}.

U images (13″ × 9″), as well as images tapered to a resolution of the order of 30″ × 20″. We did not detect any significant polarized signal in the source. The upper limit (1σ = 15 μJy b^{-1}) to the fractional polarization is ∼2–3% in the brightest regions of the halo (i.e. clumps and filaments) and ∼15% in the faintest regions, where the average total intensity emission is about 0.15 mJy. This is consistent with the polarization properties of radio halos, which are unpolarized and have upper limits of the order of few percent (Govoni et al. 2005), and confirms that A 2255 is an exceptional case.

3.3. Morphology at 240 MHz

In Fig. 3, we present the image of radio halo at 240 MHz, after subtraction of the individual radio galaxies. The image is overlaid with the X-ray emission from Chandra (see Sect. 4 for details). The 240 MHz image was convolved with a circular beam of *HPBW* = 35″ and has a sensitivity of 1σ = 400 mJy b^{-1}. The morphology of the halo at this frequency is very similar to that observed at 610 MHz and 1.4 GHz, both in the total extent and in the brightness distribution (Fig. 2).

The only feature that differs between the two images is a filament of radio emission, detected in the upper portion of the source, which departs from source A and extends toward the North for ∼1.6′ (∼450 kpc). This filament, barely visible at 610 MHz and almost undetected at 1.4 GHz (Fig. 2), has a steep spectrum, well represented by a single power law with $\alpha^{1.4\ \mathrm{GHz}}_{240\ \mathrm{MHz}}$ = 1.8. Very little can be said about this feature at this stage, but it deserves further investigation.

3.4. General properties of the radio halo

The overall extent and shape of the radio halo in RXC J2003.5–2323 are very similar at 240 MHz, 610 MHz, and 1.4 GHz. In Table 3 we summarize the main observational properties. All the given flux densities were obtained from images of comparable resolution (∼35″), and include the contribution of source A

Table 3. Properties of the radio halo in RXC J2003.5–2323.

$S_{1400\ \mathrm{MHz}}$ (mJy)	35 ± 2
$S_{610\ \mathrm{MHz}}$ (mJy)	97 ± 5∗
$S_{240\ \mathrm{MHz}}$ (mJy)	360 ± 18
α	1.32 ± 0.06
log $P_{1400\ \mathrm{MHz}}$ (W Hz^{-1})	25.09
Linear size (Mpc)	∼1.4
B'_{eq} (μG)	1.7

∗ VGB07.

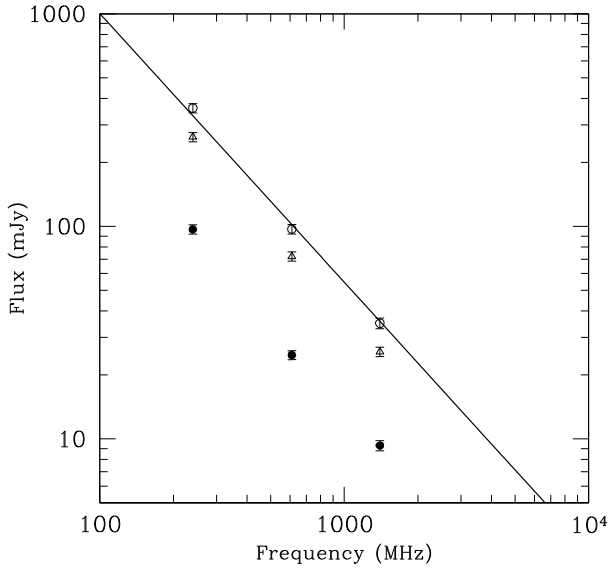

Fig. 4. Integrated radio spectrum of the halo between 240 MHz and 1.4 GHz. Filled circles are the data for source A only, empty triangles are the data for the radio halo only, and empty circles are for the radio halo+source A. The solid line is the power law fit to the data.

(Fig. 1, left panel; see also Sect. 3.1). In particular, the total flux density at 1.4 GHz was measured on the low resolution image in Fig. 2. The derived total radio power at 1.4 GHz is log $P_{1.4\ \mathrm{GHz}}$ (W Hz^{-1}) = 25.09. This value is consistent with the power of other known radio halos hosted by clusters of similar X-ray luminosity, and in agreement with the $P_{1.4\ \mathrm{GHz}} - L_{\mathrm{X}}$ correlation observed for clusters with giant radio halos (e.g., Cassano et al. 2006; Brunetti et al. 2007, and VGB07).

The spectrum of RXC J2003.5–2323 derived between 240 MHz and 1.4 GHz is shown in Fig. 4. It can be fitted by a single power law of spectral index $\alpha_{\mathrm{fit}} = 1.27^{+0.18}_{-0.08}$ (solid line in the figure), consistent with the spectral index measured in the 240–1400 MHz range (Table 3), and in line with the typical values reported in the literature for the class of giant radio halos (i.e., $\alpha \sim 1.2$–1.3; e.g., Feretti 2005). The spectral index distribution across the radio halo did not provide significant results in any frequency interval, because of the substantially different u–v coverages, which provided a patchy spectral index image with random variations around the average value.

The spectrum of source A, derived with flux density measurements obtained from the full resolution images at each of the available radio frequencies, is consistent with that of the radio halo, its spectral index being $\alpha^{1.4\ GHz}_{240\ MHz} \sim 1.3$ (see Fig. 4). The nature of this source is unclear. It is extended in the east-west direction, for a total projected size of the order of ∼410 kpc, if located at the cluster distance. Its morphology is similar to that of cluster radio galaxies; at the same time, the lack of a

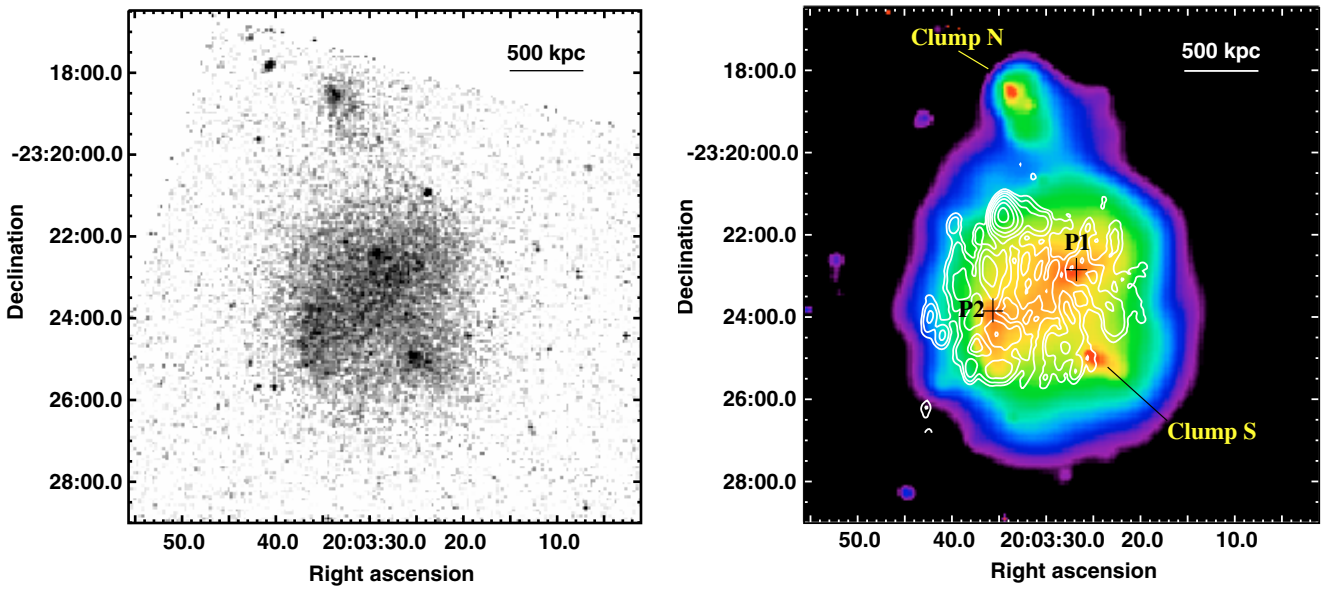

Fig. 5. *Left panel* 0.5–2.5 keV *Chandra* photon image of RXC J2003.5–2323. The image is background-subtracted, exposure-corrected, and binned to 4″ pixels. *Right panel* VLA 1.4 GHz contours (same as Fig. 1 right panel) overlaid on the 0.5−2.5 keV *Chandra* photon image smoothed with a Gaussian with $\sigma = 8''$. X-ray point sources have been subtracted.

Table 4. Details of the *Chandra* observation.

Observation mode	ACIS-I, 01236
Observing date	2007 August 2
Total exposure	50.1 ks
Effective exposure	49.8 ks

counterpart in the optical and in the near infra-red (after inspection of the SuperCOSMOS Sky Survey and of the Two Micron All Sky Survey, respectively), as well as the lack of any point-like feature in the X-ray surface brightness (see Sect. 4) suggest that it might be a peculiar bright spot in the radio halo.

We can estimate the magnetic field associated with the radio halo using the equipartition equations with a low energy cut-off of $\gamma_{\rm min} = 50$ in the particle energy spectrum (Brunetti et al. 1997), we obtain $B'_{\rm eq} = 1.7\,\mu$G (see Table 3)[2]. This is an average value, and should be considered as indicative of the entire cluster magnetic field.

4. X-ray Chandra observations and analysis

RXC J2003.5–2323 was observed by *Chandra* on 2 August 2007 with the ACIS-I detector in very faint (VF) mode. The details on the observation are listed in Table 4.

The data were reprocessed from the level 1 event files using the version 3.4 of the Chandra Interactive Analysis of Observations (CIAO) package and calibration database CALDB 3.4.2. The standard filtering was performed, excluding known bad columns, hot pixels, chip node boundaries, and events with ASCA grades 1, 5, and 7. We also applied the VF mode filtering, which significantly reduces the level of the particle background. The data were cleaned for flaring episodes using the recommendations given in Markevitch et al. (2003), leading to a useful exposure of 49.8 ks. For the background subtraction, we used the period D compilation of blank-field observations provided by Markevitch[3]. Following the prescription of Markevitch et al. (2000), the blank-field dataset was first processed identically to the dataset and then reprojected onto the sky using the aspect information and the tool MAKE_ACISBG. The resulting background file was finally renormalized to take into account the short-term and secular intensity variation in the changed particle background, which dominates the spectra at high energies. This was done by calculating the ratio of the count rates of the observation to the blank-field in the energy band of [9.5−12] keV, where the *Chandra* effective area is nearly zero, providing a normalization factor of 1.41.

4.1. Image analysis

The *Chandra* photon image of RXC J2003.5–2323 in the 0.5−2.5 keV band is presented in the left panel of Fig. 5. The image is background subtracted and divided by the exposure map. In the right panel, we show the smoothed *Chandra* image in the 0.5−5.0 keV band after subtraction of the point sources, with the radio contours at 1.4 GHz overlaid.

The cluster X-ray surface brightness distribution is clearly complex and disturbed. The central part is elongated in the south-east/north-west direction. Two peaks of emission, labelled as P1 and P2, are separated by ∼2.5′ (∼700 kpc) along this axis. A bright compact clump is located in the northern region (clump N), at a projected distance of ∼1.2 Mpc from P1. A second substructure (clump S) is detected at ∼600 kpc south of P1.

Except for an overall agreement in the shape of the radio and of the X-ray emission, there is very little coincidence between the radio and the X-ray images: the S-E/N-W elongation of the inner X-ray brightness distribution, has no corresponding features in the radio halo emission, and the two peaks P1 and P2 have no association with discrete radio sources. The superposition of the radio and the X-ray emission also indicates that the two clumps N and S have no radio counterpart. The only possible hint of connection with clump N is given in Fig. 3, which shows that the radio halo emission at 240 MHz is characterized

[2] Note that if we adopt the standard equipartition equations (computed in the frequency range 10 MHz−100 GHz), to obtain $B_{\rm eq} = 0.5\,\mu$G.

[3] http://cxc.harvard.edu/contrib/maxim/acisbg/data/

by a steep spectrum filament extending from source A towards clump N.

4.2. Spectral analysis

The spectral analysis was carried out using the version 12.2 of the X-ray spectral fitting package (XSPEC). After the detection and removal of the point sources within the cluster emission, we extracted the spectra from the selected regions of both the observation and the background. We then created the relative redistribution matrix file (RMF) and auxiliary response file (ARF). The spectra were grouped to obtain at least 20 counts per channel, and fitted using XSPEC with an absorbed single temperature thermal model (WABS*MEKAL). The fit was performed in the energy range [0.6–8] keV.

We determined the global properties of the cluster by extracting the spectrum from a circular region of radius $r = 4'$ (i.e. ∼1.1 Mpc) centered on the surface brightness centroid (RA_{J2000} = 20h03m29s, $Dec_{J2000} = -23°23'36''$). The fit was made by fixing the redshift to $z = 0.317$ and the hydrogen absorption column to the Galactic value ($N_H = 8.57 \times 10^{20}$ cm^{-2}) and allowing both the chemical abundance Z and the temperature T to vary. We found $T = 9.1^{+0.7}_{-0.6}$ keV and $Z = 0.27 \pm 0.10$. We also allowed N_H to vary and found that the fitted value of $N_H = (9.30 \pm 1.73) \times 10^{20}$ cm^{-2} is perfectly consistent with the Galactic value. The temperature found for this cluster is consistent with the values known in the literature for clusters hosting giant radio halos (Cassano et al. 2006).

4.3. Hardness ratio image

Given the complex structure of the X-ray surface brightness distribution of the cluster (Fig. 5), we searched for possible substructures in the gas temperature distribution. We produced the hardness ratio image of the cluster using the two photon images in the 0.2–2.5 keV (*soft*) and 2.5–7.0 keV (*hard*) energy bands, both background subtracted and vignetting corrected. After removing the point sources, the *soft* and *hard* images were adaptively smoothed, using the same smoothing scale pattern (map). The smoothing scale map was obtained by applying the CIAO command *csmooth* to the *soft* image requesting a minimum and a maximum significance of the signal under the smoothing kernel of 7σ and 10σ, respectively. The resulting smoothed images were combined as (*soft* – *hard*)/(*soft* + *hard*) to obtain the hardness ratio image shown in Fig. 6. The contours are obtained from the smoothed *soft* image. Finally we converted the hardness ratio values in the corresponding gas temperatures by simulating a number of absorbed single temperature thermal models with XSPEC. The result of the conversion is reported on the color bar of Fig. 6.

The hardness ratio map clearly shows that RXC J2003.5–2323 has a complex thermal structure: it lacks a central cool core, and contains a number of hot clumps. The brightest innermost cluster region is hot, with $\langle T \rangle \sim 8$–9 keV. The two X-ray peaks P1 and P2 have slightly different temperatures: the western peak P1 has $T \approx 8$ keV, while the eastern peak P2 has $T \approx 6$ keV. Clump N, instead, is much colder ($\lesssim$3 keV) than the average temperature of the cluster, while clump S has a temperature of ∼5 keV. A number of other peaks are visible in Fig. 6, although because of the low number of counts they are less significant.

To test the significance of the substructure observed in the hardness ratio image, we also extracted the spectra from the white circles shown in Fig. 6. The results, summarized in Table 5 and shown in Fig. 7, clearly show that the detected thermal structures are highly significant, confirming the unrelaxed status of this cluster. We point out that the temperatures given for P1 and P2 should be considered as estimates, which we derived from the hardness ratio image, since the statistics here are too low to fit them as separate regions.

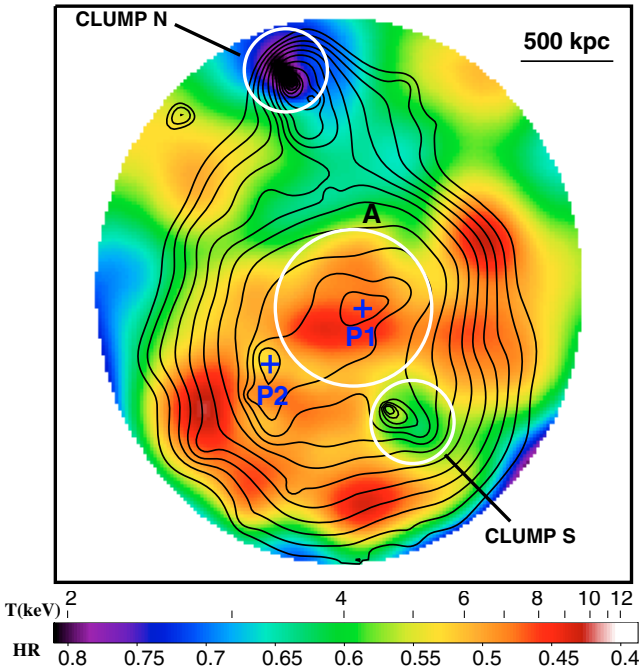

Fig. 6. Hardness ratio image of RXC J2003.5–2323. The smoothed image of the cluster in the 0.5–2.5 keV band is overlaid as contours, logarithmically spaced by a factor $\sqrt{(2)}$ (point sources were removed). The regions used for the spectral fitting, and the temperature calibration are reported.

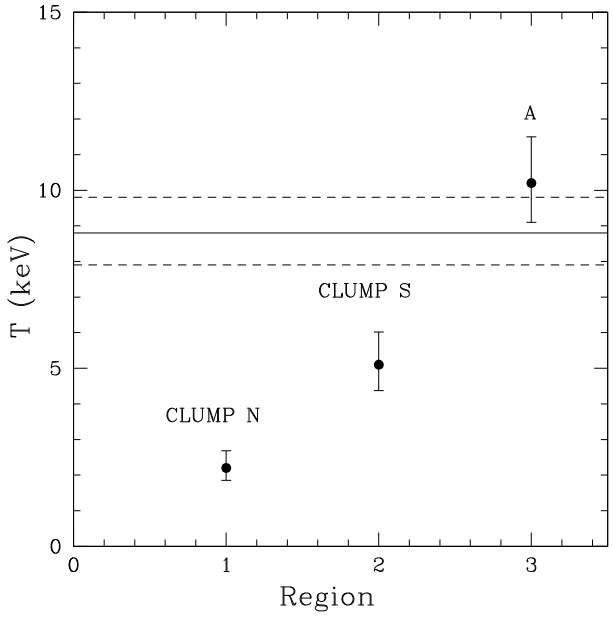

Fig. 7. Best-fit temperature of the regions defined in *the right panel* of Fig. 6. The solid line is the average temperature of the cluster (Table 5); the dashed lines delimit its error range at 90% confidence interval.

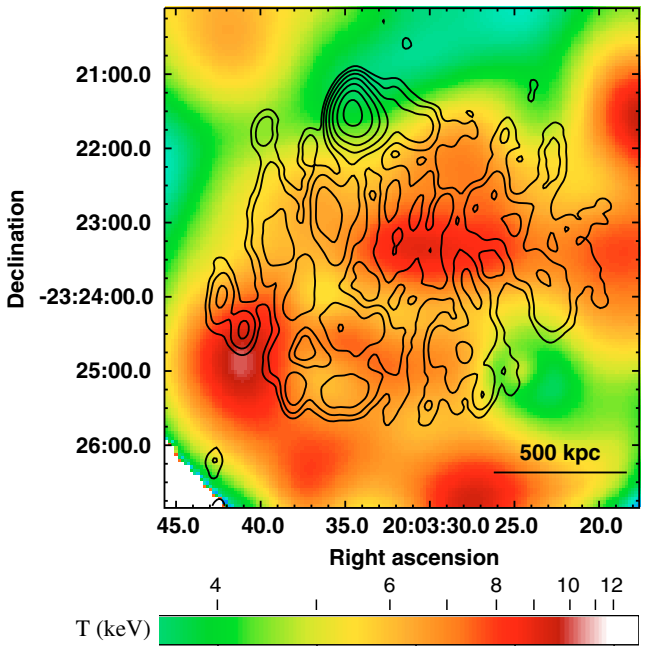

Fig. 8. Radio halo contours at 1.4 GHz (same as *right panel* of Fig. 1) on the hardness radio image of RXC J2003.5–2323 (same as Fig. 6).

Table 5. Temperatures of substructures.

Region	T (keV)	$\chi^2_{\rm red}$	Null-hyp. prob.
Clump N	$2.2^{+0.5}_{-0.3}$	0.72	0.784
Clump S	$5.1^{+0.9}_{-0.7}$	0.69	0.747
Region A	$10.2.^{+1.3}_{-1.1}$	0.99	0.544

As a further comparison in our analysis, in Fig. 8 we overlaid the radio halo contours at 1.4 GHz on the hardness ratio image, and concluded that the two images are overall independent.

5. Optical observations

We observed the cluster on the night of 6 April 2007 with the EMMI instrument of the New Technology Telescope (NTT) at the ESO La Silla Observatory (Chile). The exposure time was 300 s with the R Johnson-Cousin filter. The image was analysed with the standard bias subtraction and flat-fielding, and the SEXTRACTOR code (Bertin & Arnouts 1996) was used to extract a source catalogue. The magnitude calibration was done on the basis of the reference stars present in the field. We extracted 1059 objects with the SEXTRACTOR parameter "classstar" <0.2 (to eliminate star contamination) and with $R < 23.3$ (value at which the magnitude histogram starts to decrease).

We studied the substructure by means of the DEDICA algorithm (Bardelli et al. 1998; Pisani 1996), and restricted the analysis to the projected two dimensional distribution of the galaxies. The presence of background (i.e., non-cluster) galaxies is represented as a flat distribution within the image, therefore they do not influence the grouping algorithm and can be considered as an additional contribution to the noise. To increase the signal, we weighted all galaxies by their magnitude, if $18.3 < R < 23.3$. This approach allows to emphasize the presence of the most likely cluster members (the brightest central objects) with respect to the fainter background ones. In practice, assuming an approximately constant mass-to-light ratio, our light-weighted procedure provides a better estimate of the mass distribution.

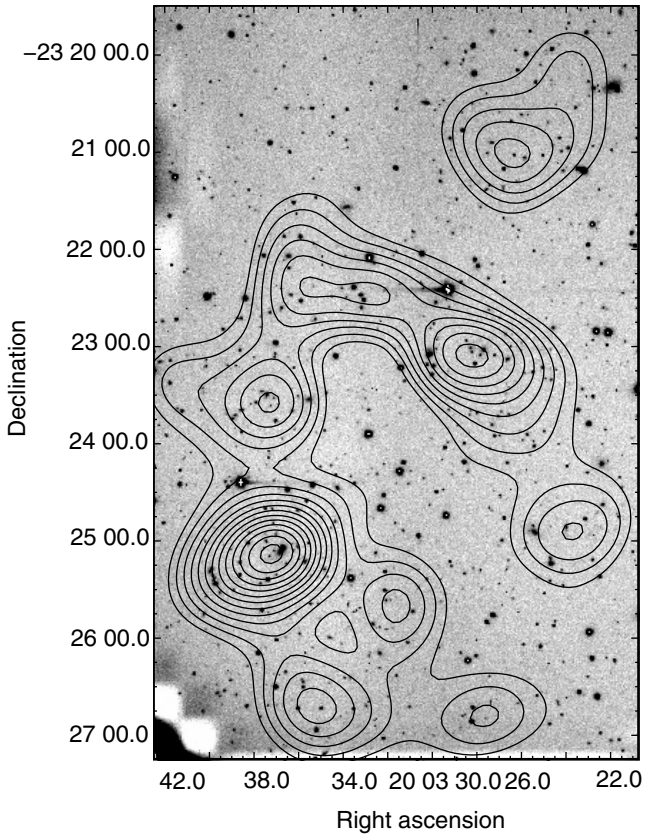

Fig. 9. Luminosity-weighted isodensity contours superimposed on our NTT R image of RXC J2003.5–2323.

In Fig. 9, we show the luminosity-weighted isodensity contours superimposed on our R image. All peaks defined by more than three isodensity contours are significant at the 99.5% level. The richest condensation is located at RA = $20^{\rm h}03^{\rm m}37^{\rm s}$ and Dec = $-23°25'08''$ and is centered on a galaxy, which could be considered the Brightest Cluster Galaxy. The second is located at RA = $20^{\rm h}03^{\rm m}28^{\rm s}$ and Dec = $-23°23'05''$, at ∼3′ (corresponding to ∼0.8 Mpc) from the main condensation. Considering a circle of 0.8 arcmin around the centers of these two condensations, the enclosed luminosty density of the western group is ∼80% that of the eastern one.

Inspection of the superposition between the X-ray surface brightness distribution on the optical luminosity-weighted contours, given in the left panel of Fig. 10, is very insightful. The central X-ray elongation and the two main optical condensations are aligned along the same axis. The X-ray peak P1 is coincident with the western optical group, while there is an offset between P2 and the Eastern most massive optical condensation.

An optical group is found to coincide with clump S, while no optical overdensity was found to coincide with the X-ray clump N, as is clear from the left panel of Fig. 10. The right panel of Fig. 10 shows the luminosity-weighted isodensity contours overlaid on the hardness ratio image. The two main optical condensations exhibit an offset with respect to the peaks in the hardness ratio. The comparison between the optical image and the radio halo shows that no features in the radio halo coincide with the main optical condensations.

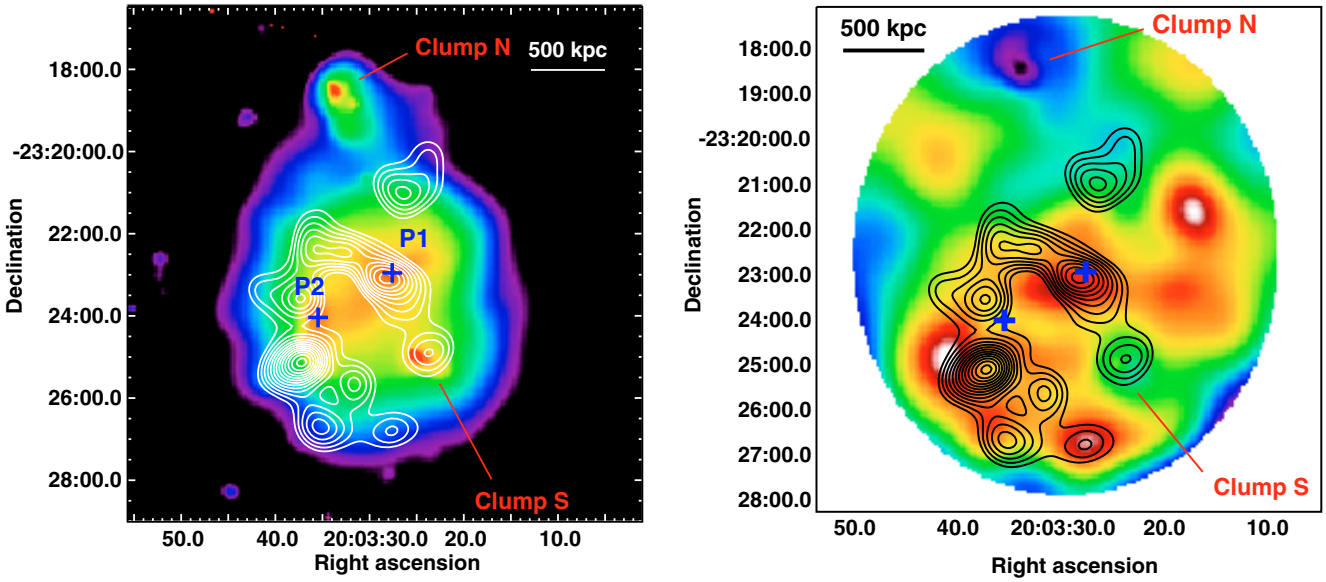

Fig. 10. Luminosity-weighted isodensity contours of the optical galaxy distribution, overlaid on the 0.5–2.5 keV smoothed *Chandra* image (*left panel*; X-ray point sources have been subtracted) and hardness ratio image of RXC J2003.5–2323 (*right panel*; same as Fig. 6).

The redshift of this cluster was estimated by Böhringer et al. (2004) on the basis of four galaxies to be $z = 0.3171$. During our observing run, we obtained the spectra for 5 more cluster galaxies, measuring the mean redshift of RXC J2003.5–2323 of $\langle z \rangle = 0.314 \pm 0.003$, which is consistent with the published value assuming a similar error for the literature data.

6. Discussion

Our multifrequency study of the cluster of galaxies RXC J2003.5–2323 has confirmed that it is in a complex dynamical state, and provides important information about the origin of its giant radio halo, whose discovery was reported in VGB07. The main observational results derived from our radio analysis can be summarized as follows:

(1) The high sensitivity GMRT and VLA radio observations confirm that it is one of the largest, most powerful, and most distant giant radio halos known so far.
(2) The radio halo is characterized by a very irregular surface brightness distribution, with clumps and filaments.
(3) The synchrotron radio spectrum is well fitted by a single power law with a spectral index $\alpha^{1.4\ \mathrm{GHz}}_{240\ \mathrm{MHz}} = 1.27^{+0.18}_{-0.08}$, consistent with the typical values of the radio halos known in the literature.
(4) It is unpolarized with an upper limit to its polarization of the order of ∼2−3%.

We now discuss the multiband properties of RXC J2003.5–2323 and the possible origins of its radio halo in the framework of the reacceleration scenario.

6.1. Dynamical state of the cluster and the radio halo/cluster merger scenario

Radio halos are always found in merging galaxy clusters, and this observational evidence provides strong constraints on the theoretical models of the formation of these structures. Based on our observations, our X-ray and optical analysis suggests that RXC J2003.5–2323 also hosts a cluster merging event. In particular, the main X-ray observational properties are:

– The X-ray brightness distribution shows substructure, as typical in dynamically unrelaxed clusters. It is elongated in the NW-SE direction, with two peaks, P1 and P2, aligned in this direction, and separated by ∼0.8 Mpc. Two more clumps of emission, N and S, have been identified in the outer regions of X-ray emission, aligned in a direction almost orthogonal to that of P1 and P2.
– The cluster X-ray temperature, $T = 9.1^{+0.7}_{-0.6}$ keV, is consistent with what is found in clusters hosting giant radio halos.
– Temperature gradients were detected in the X-ray gas distribution. The central region, which peaks at P1, has a temperature as high as 10.2 keV, while the temperature in the two clumps N and S drops to 2.2 and 5.1 keV. This result is consistent with the complex thermal structure detected by the hardness ratio analysis.

The optical analysis provides the following results:

– Our spectral data confirm that the cluster is located at a redshift $\langle z \rangle = 0.314 \pm 0.003$.
– The galaxy luminosity-weighted distribution shows two condensations, aligned along the NW-SE direction. The NW peak is located in coincidence with peak P1 in the X-ray surface brightness distribution, while the SE peak, which is also the most massive, is slighlty offset with respect to P2, although aligned along the same direction.
– A filament of galaxies connects the two optical peaks. An optical condensation was found to concide with clump S, while we found no optical overdensity associated with clump N, based on our single-band image.

A comparison of the optical and X-ray properties supports the existence of dynamical activity. In particular, the shift between the location of the X-ray peak P2 and the most massive optical condensation, clearly visible in the left panel of Fig. 10, is intriguing, as well as the relative shifts among P2, the optical clump and the peak in the hardness ratio image. We

thus conclude that the overall optical and X-ray properties of RXC J2003.5–2323 are consistent with a scenario where major merging is taking place in this cluster.

An optical/X-ray shift has been observed in the bullet cluster (1E 0657–56, Markevitch et al. 2004, and references therein) and in MACS J0025.4–1222 (Bradač et al. 2008), and has been interpreted as the result of a galaxy subcluster exiting the core of the main cluster, just ahead of the gas. In the case of RXC J2003.5–2323, it is possible that the main optical condensation is just emerging southeast after the merger, leaving the gas behind.

6.2. Origin of the radio halo morphology

Giant radio halos typically exhibit a fairly regular and homogeneous morphology, and a flux density distribution that is usually peaked at the cluster center and smoothly decreases towards the cluster periphery (e.g., A 2163; Feretti et al. 2001). The shape and extent of the radio halo in RXC J2003.5–2323 is in agreement with the X-ray surface brightness emission, although its radio flux density distribution shows clumps and filaments at all frequencies (Figs. 1–3). This morphology questions the connection with the ICM distribution.

In the framework of the reacceleration model, powerful giant radio halos at $z > 0.3$ should be hosted by massive, highly turbulent, and dynamically disturbed clusters (Cassano et al. 2006). The clumpy radio emission in RXC J2003.5–2323 may be driven both by the distribution of the emitting relativistic particles, and by that of the magnetic field intensity in the ICM.

RXC J2003.5–2323 is at relatively high redshift, where inverse Compton losses are strong and acceleration could produce synchrotron emission preferentially in regions with $B \sim B_{\rm cmb}$, where $B_{\rm cmb}$ is defined as $B_{\rm cmb} \sim 3(1+z)^2\,\mu$G. As a matter of fact, synchrotron emission from lower B would require the acceleration of electrons with significantly lower energy, while larger B would increase synchrotron losses making the acceleration process less efficient. At the same time, RXC J2003.5–2323 could be in an early merging phase and both the magnetic field and turbulence may have a filamentary structure, which are traced by the synchrotron radiation.

Another interpretation of the origin of the Mpc scale diffuse emission in RXC J2003.5–2323 is that it is a relic seen in face-on projection. However, this possibility seems very unlikely, because of the lack of polarization and to the overall spatial connection between the radio emission, X-ray surface brightness and galaxy distribution.

7. Summary and conclusions

We have presented a multifrequency study of the galaxy cluster RXC J2003.5–2323, which hosts one of the most distant, largest, and most powerful radio halos known to date, to test the cluster merger-radio halo connection.

The radio halo was imaged and analysed at high sensitivity using the VLA at 1.4 GHz, in combination with new GMRT data at 240 MHz and previously published GMRT data at 610 MHz (VGB07). The halo extends to a scale of the order of ∼1.4 Mpc at all frequencies, and its overall radio morphology is very similar in all images. The most striking feature of this source is its complex and uncommon radio brightness distribution, with clumps and filaments of emission extending to scales of the order of hundreds of kpc, which are clearly visible at all radio frequencies. This radio morphology is very different from what is found in giant radio halos, whose radio flux density generally peaks at the cluster center and smoothly decreases towards the outskirts.

Our X-ray and optical analysis suggest that the cluster is in a merging stage. In particular, our *Chandra* observations show that the cluster is very unrelaxed, with substructure in the X-ray surface brightness distribution, in the temperature and hardness ratio. An optical analysis based on ESO-NTT observations shows that the galaxy distribution is characterized by two peaks connected by a filament of galaxies, the southeastern peak considerably more massive than the northwestern one. The galaxy distribution is in reasonable agreement with the substructure in the X-ray surface brightness emission and in the hardness ratio image. A misplacement between the X-ray peak P2 and the main optical condensation suggests that the latter might be emerging southeast after the merger event, leaving the gas behind.

The clumpy and filamentary morphology of the radio halo was discussed in the framework of the reacceleration model. Because of the relatively high redshift of the cluster, which could be in an early merging phase, it is likely that the observed clumps and filaments trace the peaks of the magnetic field intensity and turbulence in the cluster.

Acknowledgements. We thank the staff of the GMRT for their help during the observations. The GMRT is run by the National Centre for Radio Astrophysics of the Tata Institute of Fundamental Research. The optical data were obtained with the European Southern Observatory NTT telescope, La Silla, Chile, program 079.A–0191(A). We acknowledge financial contribution from the Italian Ministry of Foreign Affairs, from MIUR grants PRIN2004, PRIN2005 and 2006, from PRIN–INAF2005 and from contract ASI–INAF I/023/05/01.

References

Bardelli, S., Pisani, A., Ramella, M., et al. 1998, MNRAS, 300, 589
Bertin, E., & Arnouts, S. 1996, A&AS, 117, 393
Böhringer, H., Schuecker, P., Guzzo, L., et al. 2004, A&A, 425, 367
Bradač, M., Allen, S. W., Treu, T., et al. 2008, ApJ, 687, 959
Brunetti, G. 2008, in Magnetic Fields in the Universe II, Rev. Mex. Astron. Astrof., ed. A. Esquivel, in press [arXiv:0810.0692]
Brunetti, G., Setti, G., & Comastri, A. 1997, A&A, 325, 898
Brunetti, G., Setti, G., Feretti, L., & Giovannini, G. 2001, MNRAS, 320, 365
Brunetti, G., Venturi, T., Dallacasa, D., et al. 2007, ApJ, 670, L5
Buote, D. A. 2001, ApJ, 553, L15
Cassano, R. 2009, in The Low Frequency Radio Universe, ed. D. J. Saikia, D. Green, Y. Gupta, & T. Venturi, ASP Conf. Ser., in press [arXiv:0902.2971]
Cassano, R., Brunetti, G., & Setti, G. 2006, MNRAS, 369, 1577
Feretti, L. 2003, in Texas in Tuscany, XXI Symposium on Relativistic Astrophysics, ed. R. Bandiera, R. Maiolino, & F. Mannucci (World Scientific Publishing), 209
Feretti, L. 2005, in X-ray and radio connnections, published electroncally by NRAO, ed. L. O. Sjouwerman, & K. K. Dyer
Feretti, L., Fusco-Femiano, R., Giovannini, G., et al. 2001, A&A, 373, 106
Ferrari, C., Govoni, F., Schindler, S., et al. 2008, Space Sci. Rev., 134, 93
Giacintucci, S., Venturi, T., Brunetti, G., et al. 2005, A&A, 440, 867
Giacintucci, S., Venturi, T., Macario, G., et al. 2008, A&A, 486, 347
Govoni, F., Ensslin, T. A., Feretti, L., et al. 2001, A&A, 369, 441
Govoni, F., Markevitch, M., Vikhlinin, A., et al. 2004, ApJ, 605, 695
Govoni, F., Murgia, M., Feretti, L., et al. 2005, A&A, 430, 5
Markevitch, M., Ponman, T. J., Nulsen, P. E. J., et al. 2000, ApJ, 541, 542
Markevitch, M., Bautz, M. W., Biller, B., et al. 2003, ApJ, 583, 70
Markevitch, M., Gonzalez, A. H., Clowe, D., et al. 2004, ApJ, 606, 819
Petrosian, V. 2001, ApJ, 557, 560
Pisani, A. 1996, MNRAS, 278, 697
Venturi, T., Giacintucci, S., Brunetti, G., et al. 2007, A&A, 463, 937 (VGB07)
Venturi, T., Giacintucci, S., Dallacasa, D., et al. 2008, A&A, 484, 327 (VGD08)